scientific reports

OPEN

Spin and valley dependent transport and tunneling magnetoresistance in irradiated ferromagnetic WSe$_2$ double barrier junctions

Ming Li✉, Zheng-Yin Zhao & Jia-Yi Sheng

Spin and valley polarizations (P_s and $P_{KK'}$) and tunneling magnetoresistance (TMR) are demonstrated in the ferromagnetic/barrier/normal/barrier/ferromagnetic WSe$_2$ junction, with the gate voltage and off-resonant circularly polarized light (CPL) applied to the two barrier regions. The minimum incident energy of non-zero spin- and valley-resolved conductance has been derived, which is consistent with numerical calculations and depends on the electric potential U, CPL intensity $\Delta\Omega$, exchange field h, and magnetization configuration: parallel (P) or antiparallel (AP). For the P (AP) configuration, the energy region with $P_{KK'} = -1$ or $P_s = 1$ is wider (narrower) and increases with $\Delta\Omega$. As h increases, the $P_s = 1$ ($P_{KK'} = -1$ or $P_s = 1$) plateau becomes wider (narrower) for the P (AP) configuration. As U increases, the energy region with $P_{KK'} = -1$ increases first and then moves parallel to the E_F-axis, and the energy region with $P_s = 1$ for the P configuration remains unchanged first and then decreases. The energy region for TMR = 1 increases rapidly with h, remains unchanged first and then decreases as U increases, and has little dependence on $\Delta\Omega$. When the helicity of the CPL reverses, the valley polarization will switch. This work sheds light on the design of spin-valley and TMR devices based on ferromagnetic WSe$_2$ double-barrier junctions.

In recent years, monolayer transition-metal dichalcogenides (TMDCs) have attracted extensive attention for promising applications in future devices[1–4]. In TMDCs, according to the requirement of time-reversal symmetry[6–9], the conduction and valence band extrema occur at the two degenerate valleys (K, K') located at the corners of the hexagonal Brillouin zone[9], which can be broken by the helicity of light[10]. In monolayer TMDCs, because of the broken inversion symmetry and the strong spin–orbit coupling (SOC)[6], the spin and valley degrees of freedom are coupled (spin-valley locking), and the spin splitting of the valence band is opposite at the two valleys due to the time-reversal symmetry[11]. Therefore, in TMDCs, full spin and valley polarizations can be achieved, which is crucial for spintronics and valleytronics. Significantly, high-quality WSe$_2$ with strong SOC exhibits novel behaviors that differ from other TMDCs and two-dimensional materials. Moreover, a monolayer WSe$_2$ provides a suitable platform for developing novel spintronics and valleytronics devices, as it is a direct band-gap semiconductor (band gap $E_g = 0.85$ eV)[12].

Several methods have been adopted to manipulate spin and valley degrees of freedom in TMDCs. First is the peculiar magnetic field[13]. The Zeeman effect induced by the magnetic field opens different spin-dependent band gaps at the K and K' valleys, leading to spin- and valley-polarized transport in normal/ferromagnetic/normal (N/F/N) WSe$_2$ junctions[9]. Second is the magnetic modulation induced through magnetic doping[14] or proximity effect[15–20]. The magnetic proximity effect in WSe$_2$/EuS can lead to a giant valley splitting in monolayer WSe$_2$[21]. Thirdly, utilizing the optical Stark effect, the pseudomagnetic field induced by the off-resonant CPL is used to select one of the two inequivalent valleys[22–27]. The influence of the off-resonant CPL on the valley polarization in monolayer TMDCs has attracted widespread attention recently[5,12,23–25,28–30]. For example, Hao et al. predicted the quantum spin and valley Hall effects in MoS$_2$ irradiated with the off-resonant CPL[12], and Qiu et al. demonstrated that the perfect spin and valley polarizations in WSe$_2$ are caused by the off-resonant CPL and the massive SOC[28].

College of Science, Xuchang University, Xuchang 461000, China. ✉email: mingli245@163.com

Tunneling magnetoresistance (TMR) is another key topic in spintronics, which has been widely applied to storage and magnetic sensor technologies[31], magnetic random access memory[32], and hard disk drives[33]. So far, the spin- and valley-dependent transport and TMR have been investigated theoretically and experimentally in many ferromagnetic junctions based on graphene[34,35], silicene[16,17], and MoS_2[18,19,36,37]. Moreover, the spin-valley current in many ferromagnetic junctions based on silicene[38], MoS_2[37], and WSe_2[4,39,40] can also be controlled by the off-resonant CPL. Liu et al. demonstrated that the normal/barrier/normal/barrier/normal (N/B/N/B/N) WSe_2 junction modulated by the off-resonant CPL and gate voltage can function as a valley filter and valley valve device[22]. Hajati et al. found highly spin- and valley-polarized current and high TMR in the ferromagnetic/ferromagnetic/normal (F/F/N) WSe_2 junction in the presence of gate voltage and off-resonance CPL in the middle ferromagnetic region[40]. However, by designing appropriate geometric structures, it is possible to further improve or modulate the energy region of full spin and valley polarizations as well as large TMR in WSe_2 junctions. As an extension of the system and model studied in Ref.[22], here we consider the ferromagnetic/barrier/normal/barrier/ferromagnetic (F/B/N/B/F) WSe_2 junction, where the same gate voltage and off-resonance CPL are applied in the two barrier regions. The spin- and valley-resolved effective potential for electrons in each region of the F/B/N/B/F WSe_2 junction will depend on the spin and valley degrees of freedom, the helicity of the off-resonance light, and magnetization configuration. This will certainly affect the spin- and valley-resolved conductance, spin and valley polarizations, and TMR in this junction. Furthermore, to my knowledge, existing literature has not considered the tunneling properties of the F/B/N/B/F WSe_2 junction, as well as how the spin and valley polarizations and TMR in the junction depend on the exchange field, the electrostatic potential, and the strength of the off-resonance CPL.

This paper discovers full spin and valley polarizations, as well as large TMR in the F/B/N/B/F WSe_2 junction, with gate voltage and off-resonance CPL applied to the barrier regions. We demonstrate that the energy regions of full spin and valley polarizations and large TMR can be regulated by the electric potential (U), CPL intensity ($\Delta\Omega$), and exchange field (h), and discover the underlying physical mechanisms, which have not been reported in similar ferromagnetic-TMDC junctions[18]. We derived the minimum incident energy for non-zero spin- and valley-resolved conductance, and verified it through numerical calculations. The energy region for TMR = 1 increases (decreases) with h (U) and has little dependence on $\Delta\Omega$. For the P (AP) configuration, the energy region with $P_{KK'} = -1$ or $P_s = 1$ is relatively wider (narrower) and widens as $\Delta\Omega$ increases. As h increases, the energy region with $P_s = 1$ ($P_{KK'} = -1$ or $P_s = 1$) widens (narrows) for the P (AP) configuration. As U increases, the energy region with $P_{KK'} = -1$ increases first and then moves parallel to the E_F-axis, and the energy region with $P_s = 1$ for the P configuration remains unchanged first and then decreases. When the helicity of the off-resonance light reverses, the valley polarization will switch, while the spin polarization and TMR will not.

The remainder of the paper is organized as follows. In Sec. II, the theoretical model and the schematic structure of the F/B/N/B/F WSe_2 junction are presented. Sec. III studies the spin and valley polarizations along with TMR of the WSe_2 junction in the presence of off-resonant CPL and gate voltage. Finally, Sec. IV gives a summary.

Theory and model

The proposed symmetric F/B/N/B/F WSe_2 junction is shown schematically in Fig. 1, where the two barrier regions are formed by the electrostatic potential U induced by the gate voltage and illuminated by the off-resonant CPL with a frequency of Ω. An electromagnetic potential can describe the CPL as $A(t) = [E_0\sin(\pm\Omega t)/\Omega, E_0\cos(\pm\Omega t)/\Omega]$, where + (-) corresponds to the right-handed (left-handed) circular polarization, and E_0 is the amplitude of the electric field. Due to broken inversion symmetry, monolayer TMDCs exhibit valley-dependent optical interband excitation, i.e. electrons from different valleys are selectively excited by CPLs with different helicities[41]. Moreover, the magnetization orientation in the left ferromagnetic region is assumed to be always
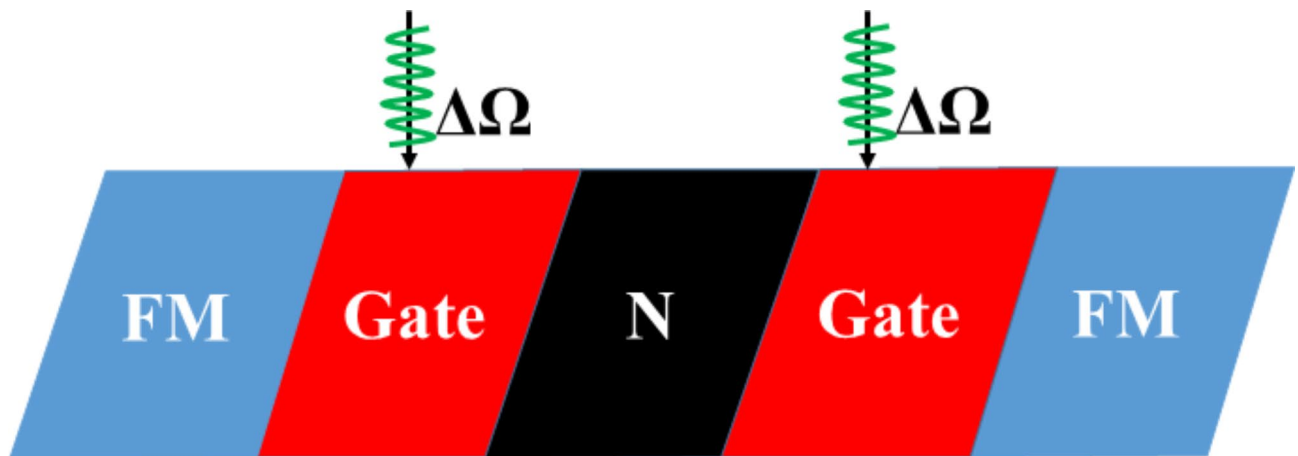

Fig. 1. Schematic diagram of WSe_2-based F/B/N/B/F junction. The two barrier regions are formed by the top gate voltage and illuminated by the off-resonant circularly polarized light.

positive, while that in the right ferromagnetic region can be positive or negative, resulting in two types of magnetization configurations: parallel (P) and antiparallel (AP).

For $eAv_f/\Omega << 1$ ($v_f = 5 \times 10^5$ m/s is the Fermi velocity in WSe$_2$), the low-energy effective Hamiltonian for the proposed WSe$_2$ junction is given by[6,22,28,42]:

$$H = \hbar v_F(k_x \tau_z \sigma_x + k_y \sigma_y) + (E_g + \tau_z \Delta\Omega)\sigma_z + \tau_z s_z(\lambda_c \sigma_+ + \lambda_v \sigma_-) + U(x) - s_z h(x) \qquad (1)$$

Here E_g is the band gap of WSe$_2$[22,39], $\Delta\Omega = (eAv_f)^2/h\Omega$ is the effective energy term describing the CPL intensity[43]. $s_z = +1$ (-1) denotes the up (down) spin of electrons, $\tau_z = +1$ (-1) stands for the K (K') valley. $\sigma_{x,y,z}$ represents the Pauli matrix in the sublattice space, and $\sigma_{\pm} = \sigma_0 \pm \sigma_z$, with σ_0 being the unit matrix[22,39]. $\lambda_c = 7.5$ meV ($\lambda_v = 112.5$ meV)[22,39] is the spin splitting at the conduction (valence) band edge caused by the intrinsic SOC. The last term in Eq. (1) represents the magnetic modulation in the ferromagnetic region, where h is the exchange field.

The electrostatic gate potential and off-resonance CPL in the two barrier regions can be defined as $U(x) = U\Theta(x)\Theta(L_B - x) + U\Theta(x - L_B - L_W)\Theta(2L_B + L_W - x)$ and $\Delta\Omega(x) = \Delta\Omega\Theta(x)\Theta(L_B - x) + \Delta\Omega\Theta(x - L_B - L_W)\Theta(2L_B + L_W - x)$, respectively, with $[\Theta(x)]$ being the Heaviside step function. Moreover, the exchange field in the two ferromagnetic regions can be described as $h(x) = h\Theta(-x) \pm h\Theta(x - 2L_B - L_W)$, where $+$ ($-$) corresponds to the P (AP) magnetization configuration.

The energy dispersion relation in the modulated regions is[22,39]:

$$E_{\pm} = \pm\sqrt{(\hbar v_F k)^2 + (E_g + \tau_z\Delta\Omega + \tau_z s_z \lambda_-)^2} + \tau_z s_z \lambda_+ + U(x) - s_z h(x) \qquad (2)$$

with $\lambda_{\pm} = \lambda_c \pm \lambda_v$. Thus the spin- and valley-resolved conduction band minimum (CBM) energy of the WSe$_2$ junction can be written as:

$$E_{\tau_z s_z} = E_g + 2\tau_z s_z \lambda_c + \tau_z \Delta\Omega(x) + U(x) - s_z h(x) \qquad (3)$$

As shown in Eqs. (2) and (3), the exchange field, off-resonance CPL, and SOC collectively lift the spin and valley degeneracy of the energy dispersion relation. Figure 2 shows the spin- and valley-resolved CBM energy (effective potential for electrons) in each region of the F/B/N/B/F WSe$_2$ junction, which depends on the spin and valley degrees of freedom and magnetization configuration, and will affect the spin- and valley-resolved conductance, spin and valley polarizations, as well as TMR of this junction. As shown in Eqs. (2) and (3), $E_{K s_z}$ ($E_{K' s_z}$) for $\Delta\Omega > 0$ approximately equals $E_{K' s_z}$ ($E_{K s_z}$) for $\Delta\Omega < 0$, because the term $|2\tau_z s_z \lambda_c| = 15$ meV is relatively small.
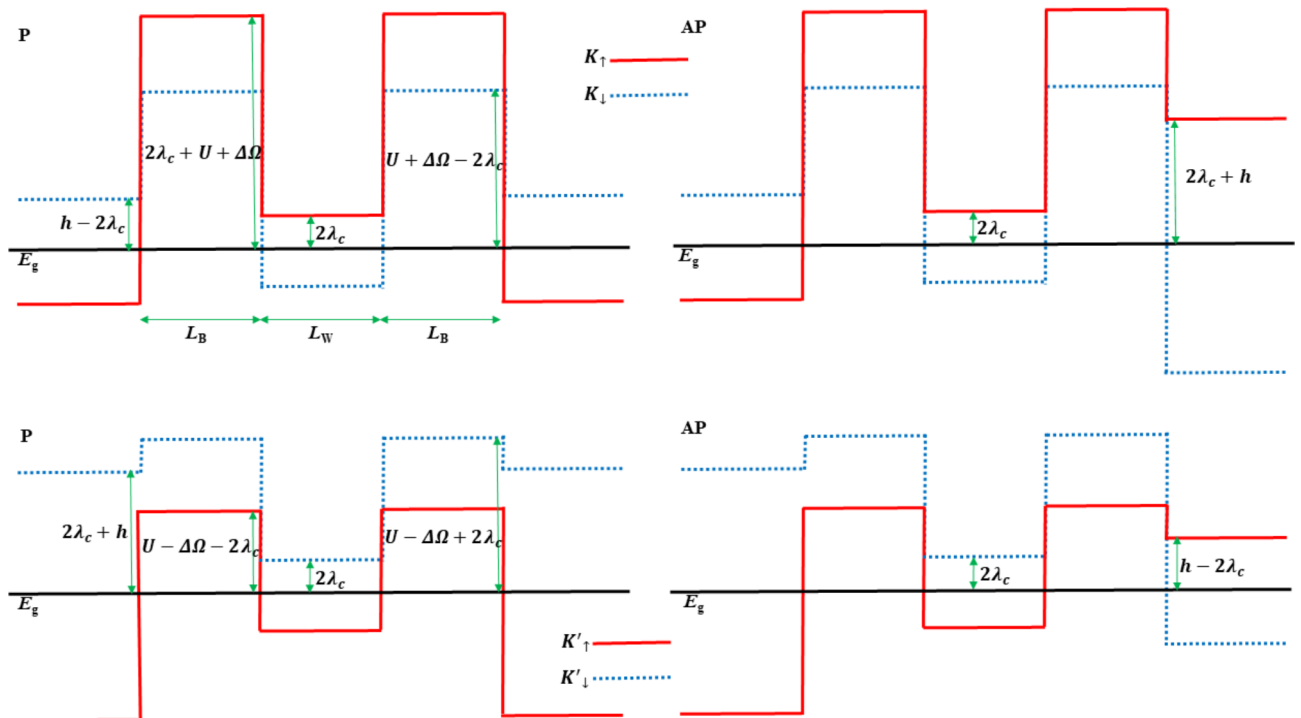

Fig. 2. Spin- and valley-resolved conduction band minimum (CBM) energy in each region of the F/B/N/B/F WSe$_2$ junction. The width of the two barrier layers is $L_B = 5$ nm, and the width of the central well layer is $L_W = 5$ nm. The left (right) column corresponds to the P (AP) configuration. The horizontal line denotes the energy level with $E = E_g = 850$ meV. ↑ (↓) denotes the up (down) spin of electrons, respectively.

Therefore, when $\Delta\Omega$ reverses the sign, the valley polarization ($P_{KK'}$) will reverse the sign synchronously, while the spin polarization (Ps) and TMR will not be deeply affected. Thus, we will only discuss the case where $\Delta\Omega > 0$.

As can be concluded from Eq. (1) and Fig. 2, the critical minimum incident energy of non-zero spin- and valley-resolved conductance ($E_{c\tau_z s_z}$) equals the highest CBM energy of the F/B/N/B/F WSe$_2$ junction, which can be expressed as follows:

$$E_{cK\uparrow} = \begin{cases} E_g + 2\lambda_c + U + \Delta\Omega & \text{for P configuration,} \\ E_g + 2\lambda_c + \max\{h, U + \Delta\Omega\} & \text{for AP configuration,} \end{cases} \qquad (4)$$

$$E_{cK\downarrow} = E_g - 2\lambda_c + \max\{h, U + \Delta\Omega\} \quad \text{for both configurations,} \qquad (5)$$

$$E_{cK'\uparrow} = \begin{cases} E_g - 2\lambda_c + \max\{0, U - \Delta\Omega\} & \text{for P configuration,} \\ E_g - 2\lambda_c + \max\{h, U - \Delta\Omega\} & \text{for AP configuration,} \end{cases} \qquad (6)$$

$$E_{cK'\downarrow} = E_g + 2\lambda_c + \max\{h, U - \Delta\Omega\} \text{ for both configurations.} \qquad (7)$$

The wave function in each region can be expressed in the following form[22]:

$$\Phi(x) = a \begin{pmatrix} 1 \\ \frac{\hbar v_F k_+}{\delta} \end{pmatrix} e^{iqx} + b \begin{pmatrix} 1 \\ \frac{\hbar v_F k_-}{\delta} \end{pmatrix} e^{-iqx} \qquad (8)$$

Here $\delta = E - U + s_z h(x) - 2\tau_z s_z \lambda_v + E_g + \tau_z \Delta\Omega$, a and b are the scattering coefficients. The parallel and perpendicular wave vectors in each region are

$$k_y = \frac{\sqrt{(E - \tau_z s_z \lambda_+ - U + s_z h(x))^2 - (E_g + \tau_z \Delta\Omega + \tau_z s_z \lambda_-)^2}}{\hbar v_F} \sin\theta$$

$$q^2 = \frac{(E - \tau_z s_z \lambda_+ - U + s_z h(x))^2 - (E_g + \tau_z \Delta\Omega + \tau_z s_z \lambda_-)^2}{(\hbar v_F)^2} - k_y^2 \qquad (9)$$

Here θ denotes the incident angle. Using the continuity condition of the wave function at the interfaces and the transfer-matrix method, the spin- and valley-dependent transmission probability ($T_{\tau_z s_z}$) can be calculated. Then, the conductance at zero temperature is given by the Landauer-Büttiker formula[44]:

$$G_{\tau_z s_z} = G_0 \int T_{\tau_z s_z} \cos\theta d\theta \qquad (10)$$

Here $G_0 = 2e^2/h$ is the quantum conductance.

The spin- and valley-resolved conductance can be written as[45,46]:

$$G_{\uparrow(\downarrow)} = \left(G_{K\uparrow(\downarrow)} + G_{K'\uparrow(\downarrow)}\right)/2 \qquad (11)$$

$$G_{K(K')} = (G_{K(K')\uparrow} + G_{K(K')\downarrow})/2 \qquad (12)$$

Using the spin- and valley-resolved conductance, the valley and spin polarizations ($P_{KK'}$ and P_s) are defined as follows[4]:

$$P_{KK'} = (G_K - G_{K'})/(G_K + G_{K'}) \qquad (13)$$

$$P_s = (G_\uparrow - G_\downarrow)/(G_\uparrow + G_\downarrow) \qquad (14)$$

Finally, TMR can be defined as[39]:

$$\text{TMR} = (G_P - G_{AP})/G_P \qquad (15)$$

Here G_P (G_{AP}) is the total conductance of the F/B/N/B/F WSe$_2$ junction in the P (AP) configuration, with $G_{P(AP)} = G_\uparrow + G_\downarrow = G_K + G_{K'}$[19].

Results and discussion

In this section, we calculate the spin- and valley-dependent conductance and TMR in the F/B/N/B/F WSe$_2$ junction for both parallel and antiparallel magnetization configurations in the presence of off-resonant CPL and gate voltage. Firstly, the cases of electric potential $U = 100$ meV, exchange field $h = 200$ meV, and different CPL intensity ($\Delta\Omega$) are explored. Secondly, the cases of $\Delta\Omega = 200$ meV, $h = 200$ meV, and different U are studied. Finally, the cases of $U = 100$ meV, $\Delta\Omega = 200$ meV, and various h are examined.

Figures 3 and 4 show the spin- and valley-resolved conductance of the F/B/N/B/F WSe$_2$ junction in P and AP configurations with $U = 100$ meV, $h = 200$ meV, and different $\Delta\Omega$. Figure 9 exhibits the corresponding total conductance as well as TMR, and Tables 1 and 2 depict the corresponding critical incident energy for the non-zero spin- and valley-resolved conductance.

For $U = 100$ meV and $h = 200$ meV, $U + \Delta\Omega > 0$ and $U - \Delta\Omega < h$ hold. So $E_{cK'\downarrow} = E_g + 2\lambda_c + h = 1065$ meV, and it is the same for both P and AP configurations and does not change with $\Delta\Omega$, as shown in Fig. 3(c) and
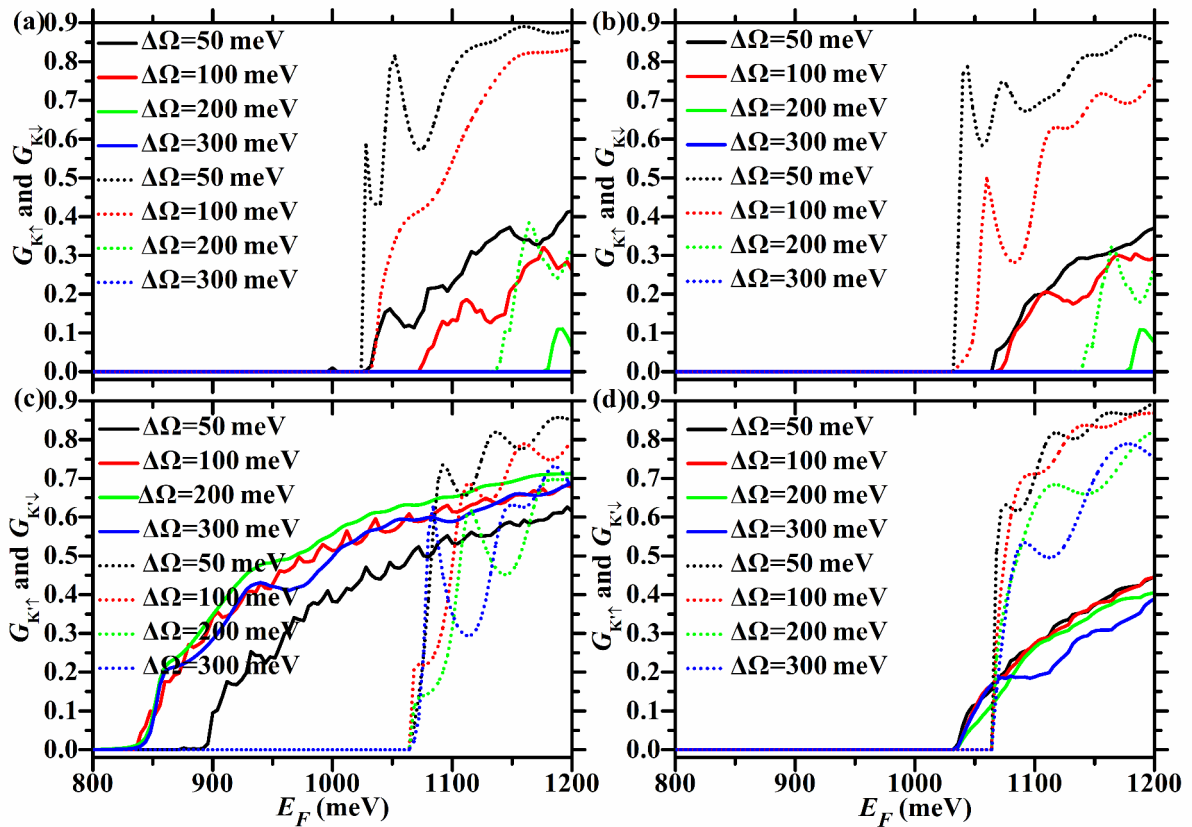
Fig. 3. Spin- and valley-resolved conductance of the F/B/N/B/F WSe$_2$ junction with $\Delta\Omega = 50, 100, 200$, and 300 meV. Here $h = 200$ meV and $U = 100$ meV. In the left (right) column, the junction is in the P (AP) configuration. The solid (dotted) lines correspond to spin-up (-down) electrons.

(d), as well as Tables 1 and 2. For the P case, $E_{cK\uparrow} = E_g + 2\lambda_c + U + \Delta\Omega = 965 + \Delta\Omega$ meV, and increases with $\Delta\Omega$, as seen in Fig. 3(a) and Table 1. For the AP case, $E_{cK'\uparrow} = E_g - 2\lambda_c + h = 1035$ meV, and does not change with $\Delta\Omega$, as illustrated in Fig. 3(d) and Table 2.

When $\Delta\Omega < 100$ meV, $U - \Delta\Omega > 0$ and $U + \Delta\Omega < h$ hold. So $E_{cK\downarrow} = E_g - 2\lambda_c + h = 1035$ meV, and it is the same for both P and AP configurations and does not vary with $\Delta\Omega$, as depicted in Fig. 3(a) and (b), as well as Tables 1 and 2.

For the P case, $E_{cK'\uparrow} = E_g - 2\lambda_c + U - \Delta\Omega = 935 - \Delta\Omega$ meV, and decreases with $\Delta\Omega$, as described in Fig. 3(c) and Table 1. So $E_{cK} = \min\{E_{cK\uparrow}, E_{cK\downarrow}\} = \min\{965 + \Delta\Omega, 1035\}$ meV, $E_{cK'} = E_{cK'\uparrow} = 935 - \Delta\Omega$ meV, $E_{c\uparrow} = E_{cK'\uparrow} = 935 - \Delta\Omega$ meV, $E_{c\downarrow} = E_{cK\downarrow} = 1035$ meV, as seen in Fig. 4(a) and (b), and Table 1. Therefore, for the P case, $P_{KK'} = -1$ in the energy region $[935 - \Delta\Omega, \min\{965 + \Delta\Omega, 1035\}$ meV], which is relatively wide and increases with $\Delta\Omega$, as shown in Fig. 4(c). $P_s = 1$ in the energy region $[935 - \Delta\Omega, 1035$ meV], which is relatively wide and increases with $\Delta\Omega$, as shown in Fig. 3(d).

For the AP case, $E_{cK\uparrow} = E_g + 2\lambda_c + h = 1065$ meV, and does not vary with $\Delta\Omega$, as seen in Fig. 3(b) and Table 2. So $E_{cK} = E_{cK\downarrow} = 1035$ meV, $E_{cK'} = E_{cK'\uparrow} = 1035$ meV, $E_{c\uparrow} = E_{cK'\uparrow} = 1035$ meV, $E_{c\downarrow} = E_{cK\downarrow} = 1035$ meV, as seen in Fig. 4(e) and (f), and Table 2. Therefore, for the AP case, the energy region with $P_{KK'} = -1$ ($P_s = 1$) does not exist, as shown in Fig. 4(g), (h).

TMR = 1 in the energy region $[935 - \Delta\Omega, 1035$ meV], which is relatively wide and increases with $\Delta\Omega$, and its upper limit does not change with $\Delta\Omega$, as shown in Fig. 9(a) and (b).

When $\Delta\Omega \geq 100$ meV, $U - \Delta\Omega \leq 0$ and $U + \Delta\Omega \geq h$ hold. So $E_{cK\downarrow} = E_g - 2\lambda_c + U + \Delta\Omega = 935 + \Delta\Omega$ meV, and increases with $\Delta\Omega$, regardless of P or AP configuration, as depicted in Fig. 3(a) and (b), as well as Tables 1 and 2.

For the P case, $E_{cK'\uparrow} = E_g - 2\lambda_c = 835$ meV, and does not vary with $\Delta\Omega$, as seen in Fig. 3(c) and Table 1. So $E_{cK} = E_{cK\downarrow} = E_g - 2\lambda_c + U + \Delta\Omega = 935 + \Delta\Omega$ meV, $E_{cK'} = E_{cK'\uparrow} = E_g - 2\lambda_c = 835$ meV, $E_{c\uparrow} = E_{cK'\uparrow} = E_g - 2\lambda_c = 835$ meV, $E_{c\downarrow} = \min\{935 + \Delta\Omega, 1065\}$ meV, as seen in Fig. 4(a) and (b) and Table 1. For the P case, $P_{KK'} = -1$ in the energy region $[835, 935 + \Delta\Omega$ meV], which is relatively wide and increases with $\Delta\Omega$, as seen in Fig. 4(c). As shown in Fig. 4(d), $P_s = 1$ in the energy region $[835, \min\{935 + \Delta\Omega, 1065\}$ meV]. This increases with $\Delta\Omega$ when $100 < \Delta\Omega < 130$ meV, and remains at $[835, 1065$ meV] when $\Delta\Omega \geq 130$ meV, with a width of 230 meV.
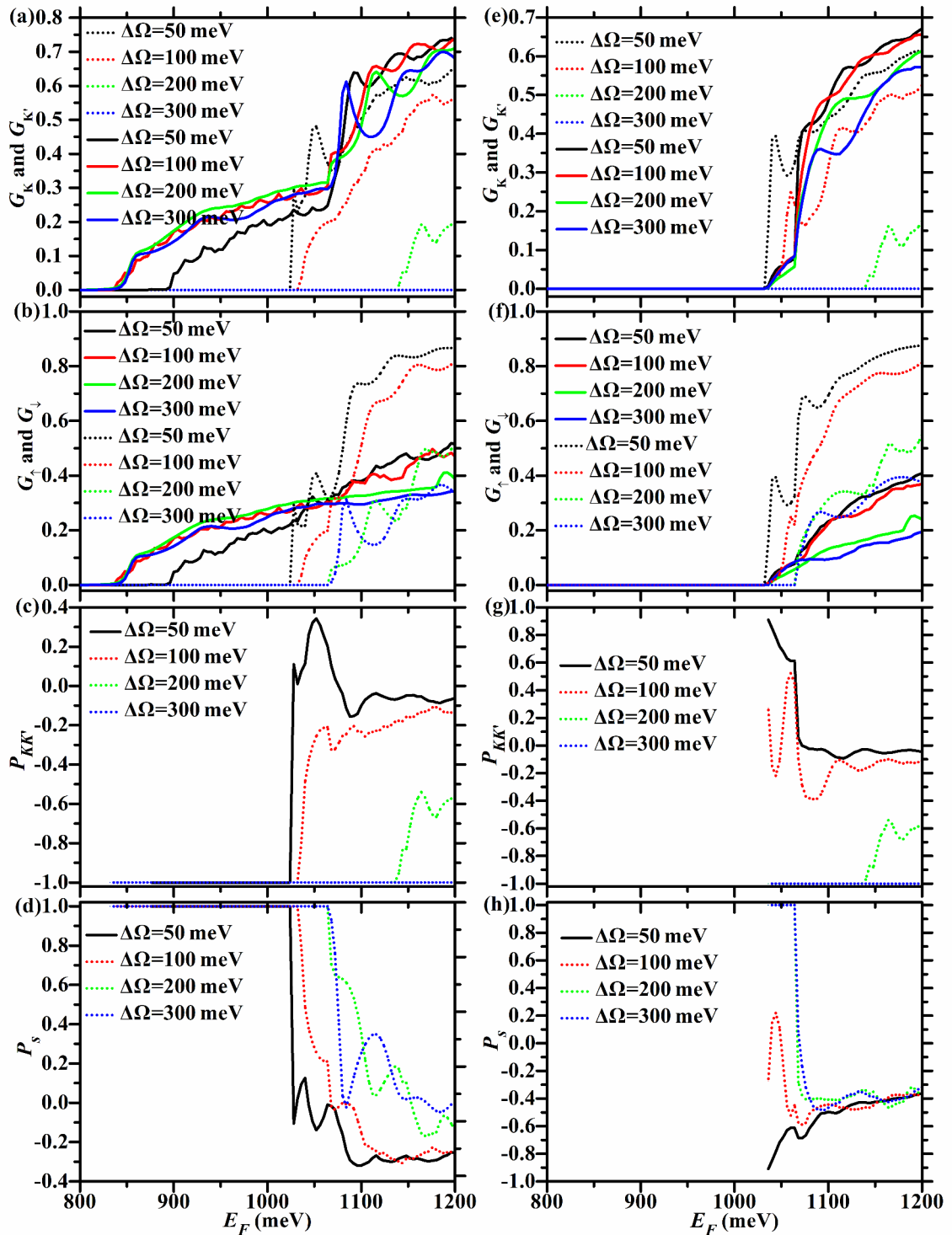
Fig. 4. G_K (dotted lines), $G_{K'}$ (solid lines), $G\uparrow$ (solid lines), $G\downarrow$ (dotted lines), $P_{KK'}$, and P_s versus E_F for the F/B/N/B/F WSe$_2$ junction with $\Delta\Omega = 50$, 100, 200, and 300 meV. Here $h = 200$ meV and $U = 100$ meV. In the left (right) column, the junction is in the P (AP) configuration.

For the AP case, $E_{cK\uparrow} = E_g + 2\lambda_c + U + \Delta\Omega = 965 + \Delta\Omega$ meV, and increases with $\Delta\Omega$, as seen in Fig. 3(b) and Table 2. So $E_{cK} = E_{cK\downarrow} = 935 + \Delta\Omega$ meV, $E_{cK'} = E_{cK'\uparrow} = 1035$ meV, $E_{c\uparrow} = E_{cK'\uparrow} = 1035$ meV, $E_{c\downarrow} = \min\{935 + \Delta\Omega, 1065\}$ meV, as seen in Fig. 4(e) and (f) and Table 2. For the AP case, $P_{KK'} = -1$ in the energy region [1035, 935 + $\Delta\Omega$ meV], which increases with $\Delta\Omega$, as shown in Fig. 4(g). As shown in

$\Delta\Omega$	$E_{cK\uparrow}$	$E_{cK\downarrow}$	$E_{cK'\uparrow}$	$E_{cK'\downarrow}$	E_{cK}	$E_{cK'}$	$E_{c\uparrow}$	$E_{c\downarrow}$
50	1028	1028	876	1068	1028	876	876	1028
100	1076	1036	836	1068	1036	836	836	1036
200	1180	1140	812	1068	1140	812	812	1068
300	>1200	>1200	824	1068	>1200	824	824	1068

Table 1. The critical incident energy (in units of meV) of non-zero spin- and valley-resolved conductance of the F/B/N/B/F WSe$_2$ junction in the P configuration with $U = 100$ meV, $h = 200$ meV, and $\Delta\Omega = 50$, 100, 200, and 300 meV, respectively.

$\Delta\Omega$	$E_{cK\uparrow}$	$E_{cK\downarrow}$	$E_{cK'\uparrow}$	$E_{cK'\downarrow}$	E_{cK}	$E_{cK'}$	$E_{c\uparrow}$	$E_{c\downarrow}$
50	1068	1036	1036	1068	1036	1036	1036	1036
100	1068	1036	1036	1068	1036	1036	1036	1036
200	1176	1140	1036	1068	1140	1036	1036	1068
300	>1200	>1200	1036	1068	>1200	1036	1036	1068

Table 2. The critical incident energy (in units of meV) of non-zero spin- and valley-resolved conductance of the F/B/N/B/F WSe$_2$ junction in the AP configuration with $U = 100$ meV, $h = 200$ meV, and $\Delta\Omega = 50$, 100, 200, and 300 meV, respectively.

Fig. 4(h), $P_s = 1$ in the energy region [1035,min{935 + $\Delta\Omega$, 1065} meV]. This region increases with $\Delta\Omega$ when $100 < \Delta\Omega < 130$ meV, and remains at [1035,1065 meV] when $\Delta\Omega \geq 130$ meV, with a width of 30 meV.

Therefore, when $\Delta\Omega \geq 100$ meV, TMR = 1 in the energy region [835,1035 meV], which is relatively wide and remains at 200 meV, as described in Fig. 9(a) and (b).

Figures 5 and 6 show the spin- and valley-resolved conductance of the F/B/N/B/F WSe$_2$ junction in P and AP configurations with $\Delta\Omega = 200$ meV, $h = 200$ meV, and different U. Figure 9 exhibits the corresponding total conductance as well as TMR, and Tables 3 and 4 depict the corresponding critical incident energy for the non-zero spin- and valley-resolved conductance.

For $\Delta\Omega = 200$ meV and $h = 200$ meV, $U + \Delta\Omega > h$ holds. So $E_{cK\uparrow} = E_g + 2\lambda_c + U + \Delta\Omega = 1065 + U$ meV, $E_{cK\downarrow} = E_g - 2\lambda_c + U + \Delta\Omega = 1035 + U$ meV, and they are the same for both P and AP configurations and increase with U, as seen in Fig. 5(a) and (b), as well as Tables 3 and 4.

When $U < 200$ meV, $U - \Delta\Omega < 0 < h$ holds. So $E_{cK'\downarrow} = E_g + 2\lambda_c + h = 1065$ meV, and does not change with U, whether P or AP configuration, as shown in Fig. 5(c) and (d), as well as Tables 3 and 4.

For the P case, $E_{cK'\uparrow} = E_g - 2\lambda_c = 835$ meV, and does not change with $\Delta\Omega$, as seen in Fig. 5(c) and Table 3. So $E_{cK} = E_{cK\downarrow} = 1035 + U$ meV, $E_{cK'} = E_{cK'\uparrow} = 835$ meV, $E_{c\uparrow} = E_{cK'\uparrow} = 835$ meV, $E_{c\downarrow} = \min\{1065, 1035 + U\}$ meV, as illustrated in Fig. 6(a) and (b) and Table 3. Therefore, for the P case, $P_{KK'} = $ -1 in the energy region [835,1035 + U meV], which increases with U, as seen in Fig. 6(c). As shown in Fig. 6(d), $P_s = 1$ in the energy region [835,min{1065, 1035 + U} meV]. This region increases with U when $0 < U < 30$ meV, and remains at [835,1065 meV] when $30 \leq U < 200$ meV, with a width of 230 meV.

For the AP case, $E_{cK'\uparrow} = E_g - 2\lambda_c + h = 1035$ meV, and does not change with U, as seen in Fig. 5(d) and Table 4. So $E_{cK} = E_{cK\downarrow} = 1035 + U$ meV, $E_{cK'} = E_{cK'\uparrow} = 1035$ meV, $E_{c\uparrow} = E_{cK'\uparrow} = 1035$ meV, $E_{c\downarrow} = \min\{1065, 1035 + U\}$ meV, as seen in Fig. 6(e) and (f) and Table 4. For the AP case, $P_{KK'} = $ -1 in the energy region [1035,1035 + U meV], which increases with U, as seen in Fig. 6(g). As shown in Fig. 6(h), $P_s = 1$ in the energy region [1035,min{1065, 1035 + U} meV]. This region increases with U when $0 < U < 30$ meV, and remains at [1035,1065 meV] when $30 \leq U < 200$ meV, with a width of 30 meV.

Therefore, when $U < 200$ meV, TMR = 1 in the energy region [835,1035 meV], which is relatively wide and remains at 200 meV, as shown in Fig. 9(c) and (d).

When $200 \leq U < 400$ meV, $0 < U - \Delta\Omega < h$ holds. So $E_{cK'\downarrow} = E_g + 2\lambda_c + h = 1065$ meV, and it is the same for both P and AP configurations and does not vary with U, as seen in Fig. 5(c) and (d), as well as Tables 3 and 4.

For the P case, $E_{cK'\uparrow} = E_g - 2\lambda_c + U - \Delta\Omega = 635 + U$ meV, and increases with U, as seen in Fig. 5(c) and Table 3. So $E_{cK} = E_{cK\downarrow} = 1035 + U$ meV, $E_{cK'} = E_{cK'\uparrow} = 635 + U$ meV, $E_{c\uparrow} = E_{cK'\uparrow} = 635 + U$ meV, $E_{c\downarrow} = E_{cK'\downarrow} = 1065$ meV, as seen in Fig. 6(a) and (b) and Table 3. For the P case, $P_{KK'} = $ -1 in the energy region [635 + U,1035 + U meV], which is relatively wide and remains at 400 meV. As U increases, it moves parallel to the E_F-axis as a whole, as seen in Fig. 6(c). $P_s = 1$ in the energy region [635 + U,1065 meV], which decreases with U, as seen in Fig. 6(d).

For the AP case, $E_{cK'\uparrow} = E_g - 2\lambda_c + h = 1035$ meV, and does not change with U, as seen in Fig. 5(d) and Table 4. So $E_{cK} = E_{cK\downarrow} = 1035 + U$ meV, $E_{cK'} = E_{cK'\uparrow} = 1035$ meV, $E_{c\uparrow} = E_{cK'\uparrow} = 1035$ meV, $E_{c\downarrow} = E_{cK'\downarrow} = 1065$ meV, as seen in Fig. 6(e) and (f) and Table 4. For the AP case, $P_{KK'} = $ -1 in the energy region [1035,1035 + U meV], which increases with U, as seen in Fig. 6(g). As seen in Fig. 6(h), $P_s = 1$ in the energy region [1035,1065 meV], which is relatively narrow and remains at 30 meV as U increases.

Therefore, when $200 \leq U < 400$ meV, TMR = 1 in the energy region [635 + U,1035 meV], which decreases evidently with U, as shown in Fig. 9(c) and (d).
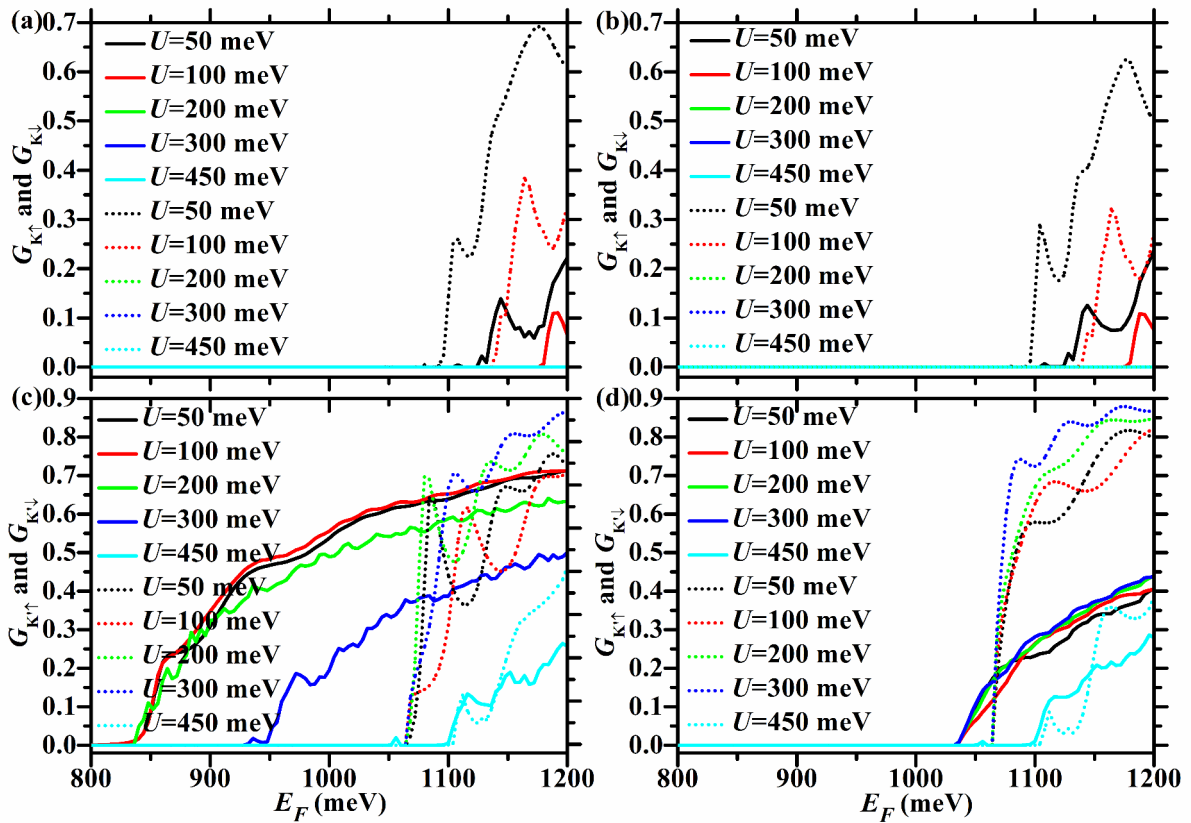
Fig. 5. Spin- and valley-resolved conductance of the F/B/N/B/F WSe$_2$ junction with $\Delta\Omega = 200$ meV, $h = 200$ meV, and $U = 50, 100, 200, 300$ and 450 meV. The solid (dotted) lines correspond to spin-up (-down) electrons. In the left (right) column, the junction is in the P (AP) configuration.

When $U \geq 400$ meV, $U - \Delta\Omega \geq h$ holds. $E_{cK'\uparrow} = E_g - 2\lambda_c + U - \Delta\Omega = 635 + U$ meV, $E_{cK'\downarrow} = E_g + 2\lambda_c + U - \Delta\Omega = 665 + U$ meV, and they are the same for both P and AP configurations and increase with U, as seen in Fig. 5(c) and (d), as well as Tables 3 and 4. So $E_{cK} = E_{cK\downarrow} = 1035 + U$ meV, $E_{cK'} = E_{cK'\uparrow} = 635 + U$ meV, $E_{c\uparrow} = E_{cK'\uparrow} = 635 + U$ meV, $E_{c\downarrow} = E_{cK'\downarrow} = 665 + U$ meV, as seen in Fig. 6(a), (b), (e), and (f) and Tables 3 and 4. Thus $P_{KK'} = -1$ in the energy region $[635 + U, 1035 + U$ meV], which is relatively wide and remains at 400 meV. As U increases, it moves parallel to the E_F-axis as a whole, as shown in Fig. 6(c) and (g). In theory, $P_s = 1$ in the energy region $[635 + U, 665 + U$ meV], which is relatively narrow and moves parallel to the E_F-axis as U increases. However, when $U = 450$ meV, as seen in Fig. 6(b) and (f) and Tables 3 and 4, $E_{c\uparrow}$ (1096 meV) and $E_{c\downarrow}$ (1100 meV) are very close, making it difficult to see the energy region with $P_s = 1$ in Fig. 6(d) and (h).

Therefore, the energy region with TMR = 1 does not exist when $U \geq 400$ meV, as described in Fig. 9(c) and (d).

Figures 7 and 8 show the spin- and valley-resolved conductance of the F/B/N/B/F WSe$_2$ junction in P and AP configurations with $U = 100$ meV, $\Delta\Omega = 200$ meV, and different h. Figure 9 exhibits the corresponding total conductance as well as TMR, and Tables 5 and 6 depict the corresponding critical incident energy for the non-zero spin- and valley-resolved conductance.

For $U = 100$ meV and $\Delta\Omega = 200$ meV, $U - \Delta\Omega < 0 < h$ holds. So $E_{cK'\downarrow} = E_g + 2\lambda_c + h = 865 + h$ meV, and it is the same for both P and AP configurations and increases with h, as described in Fig. 7(c) and (d), as well as Tables 5 and 6. For the P case, $E_{cK\uparrow} = E_g + 2\lambda_c + U + \Delta\Omega = 1165$ meV, $E_{cK'\uparrow} = E_g - 2\lambda_c = 835$ meV, and they do not change with h, as seen in Fig. 7(a) and (c) and Table 5. For the AP case, $E_{cK'\uparrow} = E_g - 2\lambda_c + h = 835 + h$ meV, and increases with h, as shown in Fig. 7(d) and Table 6.

When $h < 300$ meV, $U + \Delta\Omega > h$ holds. $E_{cK\downarrow} = E_g - 2\lambda_c + U + \Delta\Omega = 1135$ meV and does not change with h, whether P or AP configuration, as depicted in Fig. 7(a) and (b), as well as Tables 5 and 6.

For the P case, $E_{cK} = E_{cK\downarrow} = 1135$ meV, $E_{cK'} = E_{cK'\uparrow} = 835$ meV, $E_{c\uparrow} = E_{cK'\uparrow} = 835$ meV, $E_{c\downarrow} = \min\{1135, 865 + h\}$ meV, as seen in Fig. 7(a) and (b) and Table 5. Therefore, for the P case, as h increases, the energy region with $P_{KK'} = -1$ remains at $[835, 1135$ meV], which is relatively wide and remains at 300 meV, as shown in Fig. 8(c). As shown in Fig. 8(d), $P_s = 1$ in the energy region $[835, \min\{865 + h, 1135\}$ meV]. This region increases evidently with h when $0 < h < 270$ meV, and remains at $[835, 1135$ meV] when $270 \leq h < 300$ meV.
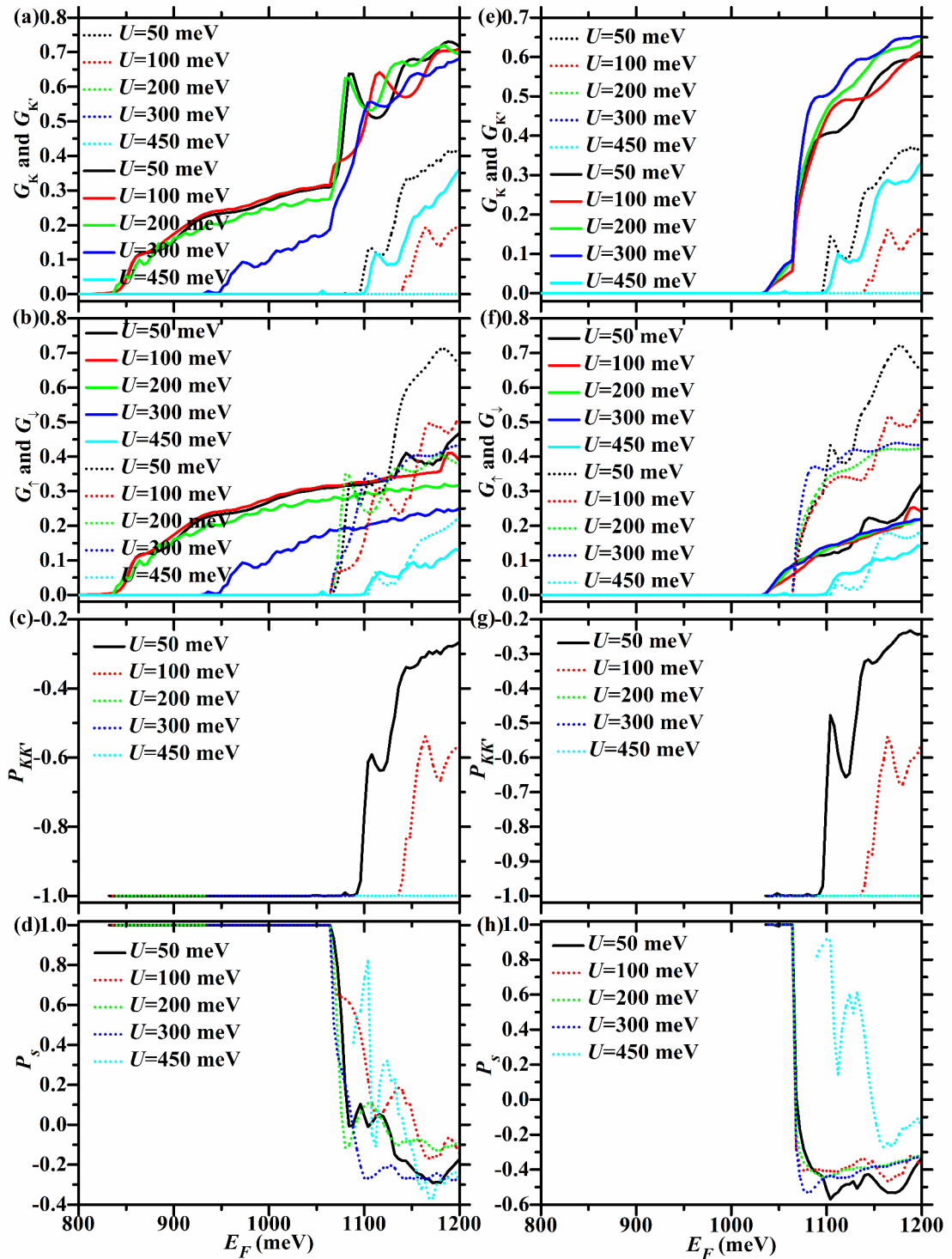
Fig. 6. G_K (dotted lines), $G_{K'}$ (solid lines), $G\uparrow$ (solid lines), $G\downarrow$ (dotted lines), $P_{KK'}$, and P_s versus E_F for the F/B/N/B/F WSe$_2$ junction with $U = 50$, 100, 200, 300, and 450 meV. Here $h = 200$ meV and $\Delta\Omega = 200$ meV. In the left (right) column, the junction is in the P (AP) configuration.

For the AP case, $E_{cK\uparrow} = E_g + 2\lambda_c + U + \Delta\Omega = 1165$ meV, and does not change with h, as shown in Fig. 7(b) and Table 6, just like in the P case. So $E_{cK} = E_{cK\downarrow} = 1135$ meV, $E_{cK'} = E_{cK'\uparrow} = 835 + h$ meV, $E_{c\uparrow} = E_{cK'\uparrow} = E_g - 2\lambda_c + h = 835 + h$ meV, $E_{c\downarrow} = \min\{1135, 865 + h\}$ meV, as seen in Fig. 8(e) and (f) and Table 6. For the AP case, $P_{KK'} = -1$ in the energy region $[835 + h, 1135$ meV$]$, which decreases evidently with h, as seen in Fig. 8(g). When $h = 300$ meV, the energy region with $P_{KK'} = -1$ disappears completely. As shown in

U	$E_{cK\uparrow}$	$E_{cK\downarrow}$	$E_{cK'\uparrow}$	$E_{cK'\downarrow}$	E_{cK}	$E_{cK'}$	$E_{c\uparrow}$	$E_{c\downarrow}$
50	1128	1092	820	1068	1092	820	820	1068
100	1180	1140	812	1068	1140	812	812	1068
200	>1200	>1200	836	1068	>1200	836	836	1068
300	>1200	>1200	932	1068	>1200	932	932	1068
450	>1200	>1200	1096	1100	>1200	1096	1096	1100

Table 3. The critical incident energy (in units of meV) of non-zero spin- and valley-resolved conductance of the F/B/N/B/F WSe$_2$ junction in the P configuration with $\Delta\Omega = 200$ meV, $h = 200$ meV, and $U = 50$, 100, 200, 300 and 450 meV, respectively.

U	$E_{cK\uparrow}$	$E_{cK\downarrow}$	$E_{cK'\uparrow}$	$E_{cK'\downarrow}$	E_{cK}	$E_{cK'}$	$E_{c\uparrow}$	$E_{c\downarrow}$
50	1108	1092	1036	1068	1092	1036	1036	1068
100	1176	1140	1036	1068	1140	1036	1036	1068
200	>1200	>1200	1036	1068	>1200	1036	1036	1068
300	>1200	>1200	1036	1068	>1200	1036	1036	1068
450	>1200	>1200	1096	1100	>1200	1096	1096	1100

Table 4. The critical incident energy (in units of meV) of non-zero spin- and valley-resolved conductance of the F/B/N/B/F WSe$_2$ junction in the AP configuration with $\Delta\Omega = 200$ meV, $h = 200$ meV, and $U = 50$, 100, 200, 300 and 450 meV, respectively.
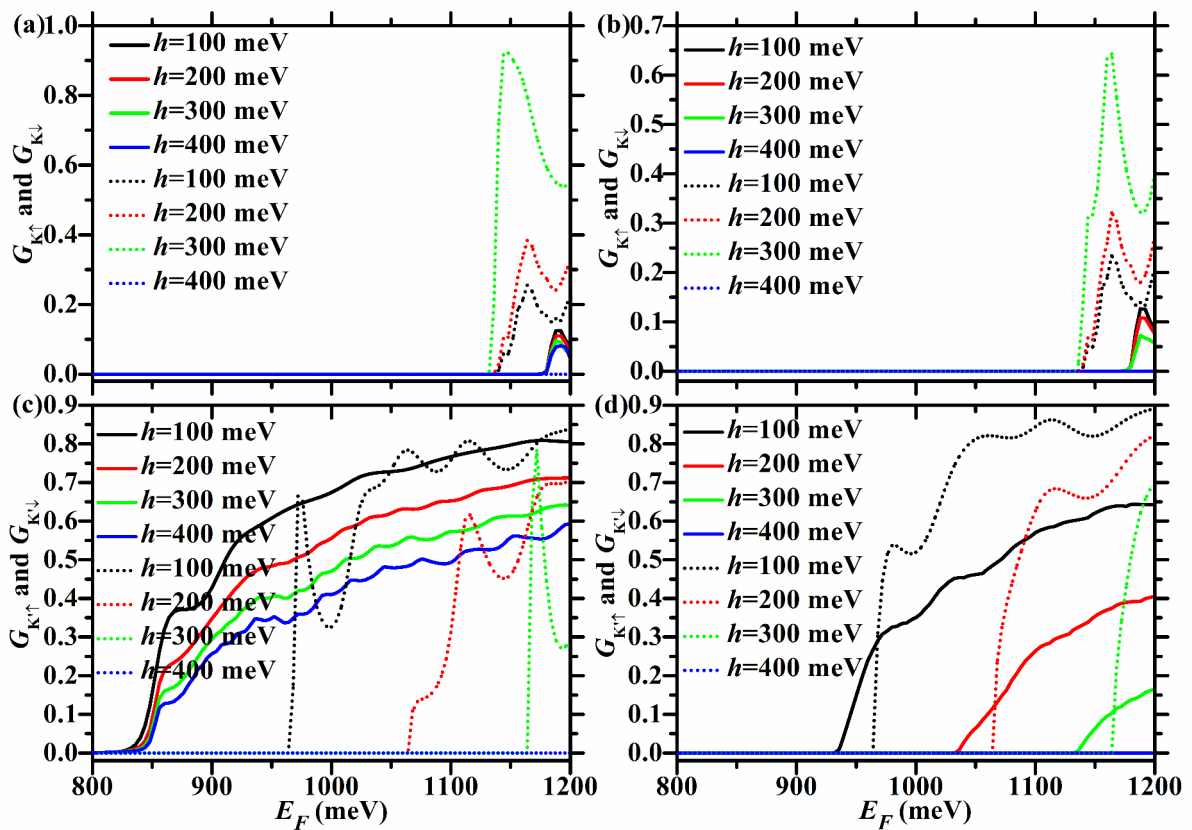
Fig. 7. Spin- and valley-resolved conductance of the F/B/N/B/F WSe$_2$ junction under different h and fixed U (100 meV) and $\Delta\Omega$ (200 meV). The solid (dotted) lines correspond to spin-up (-down) electrons. In the left (right) column, the junction is in the P (AP) configuration.
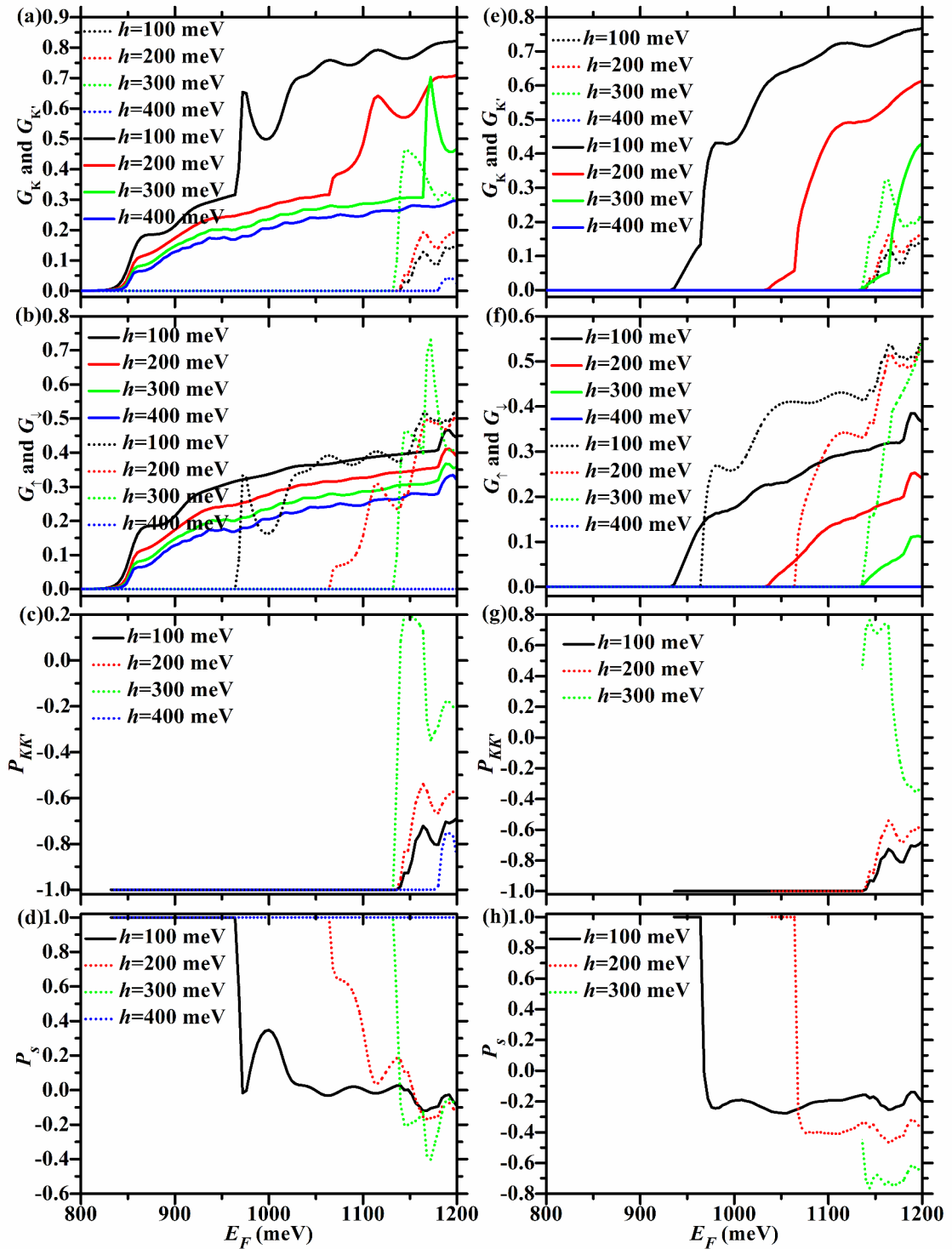
Fig. 8. G_K (dotted lines), $G_{K'}$ (solid lines), $G\uparrow$ (solid lines), $G\downarrow$ (dotted lines), $P_{KK'}$, and P_s versus E_F for the F/B/N/B/F WSe$_2$ junction with $U = 100$ meV and $\Delta\Omega = 200$ meV, $h = 100$, 200, 300, and 400 meV, respectively. In the left (right) column, the junction is in the P (AP) configuration.

Fig. 8(h), $P_s = 1$ in the energy region $[835 + h, \min\{865 + h, 1135\}$ meV$]$. When $0 < h < 270$ meV, this region remains at $[835 + h, 865 + h$ meV$]$, with a width of 30 meV. When $270 < h < 300$ meV, it decreases evidently with h. When $h = 300$ meV, it disappears completely.

Therefore, when $h < 300$ meV, TMR $= 1$ in the energy region $[835, 835 + h$ meV$]$, which is relatively wide and increases rapidly with h, as shown in Fig. 9(e) and (f).
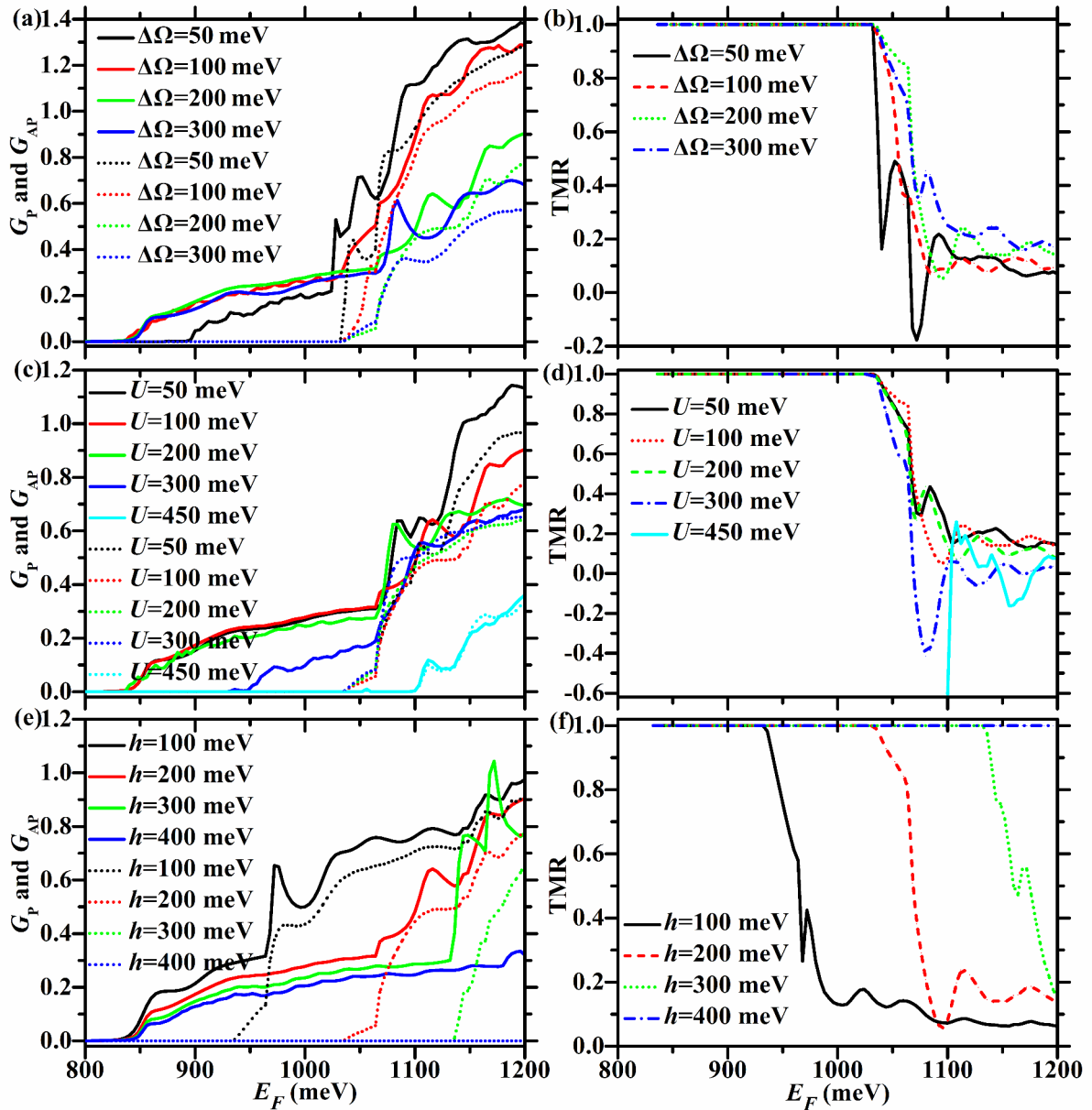
Fig. 9. The total conductance (left column) of the F/B/N/B/F WSe$_2$ junction in P and AP configurations, as well as the corresponding TMR (right column). The solid (dotted) lines correspond to the P (AP) configuration. Here $U=100$ meV and $h=200$ meV in the first row, $h=200$ meV and $\Delta\Omega=200$ meV in the second row, and $U=100$ meV and $\Delta\Omega=200$ meV in the third row.

h	$E_{cK\uparrow}$	$E_{cK\downarrow}$	$E_{cK'\uparrow}$	$E_{cK'\downarrow}$	E_{cK}	$E_{cK'}$	$E_{c\uparrow}$	$E_{c\downarrow}$
100	1180	1140	812	968	1140	812	812	968
200	1180	1140	812	1068	1140	812	812	1068
300	1180	1140	808	1168	1136	808	808	1136
400	1180	>1200	808	>1200	1180	808	808	>1200

Table 5. The critical incident energy (in units of meV) of non-zero spin- and valley-resolved conductance of the F/B/N/B/F WSe$_2$ junction in the P configuration with $U=100$ meV, $\Delta\Omega=200$ meV, and $h=100$, 200, 300, and 400 meV, respectively.

h	$E_{cK\uparrow}$	$E_{cK\downarrow}$	$E_{cK'\uparrow}$	$E_{cK'\downarrow}$	E_{cK}	$E_{cK'}$	$E_{c\uparrow}$	$E_{c\downarrow}$
100	1180	1140	936	968	1140	936	936	968
200	1176	1136	1036	1068	1140	1036	1036	1068
300	1176	1136	1136	1168	1136	1136	1136	1136
400	>1200	>1200	>1200	>1200	>1200	>1200	>1200	>1200

Table 6. The critical incident energy (in units of meV) of non-zero spin- and valley-resolved conductance of the F/B/N/B/F WSe$_2$ junction in the AP configuration with $U = 100$ meV, $\Delta\Omega = 200$ meV, and $h = 100, 200, 300,$ and 400 meV, respectively.

When $h \geq 300$ meV, $U + \Delta\Omega \leq h$ holds. So $E_{cK\downarrow} = E_g - 2\lambda_c + h = 835 + h$ meV, and increases with h, regardless of P or AP configuration, as seen in Fig. 7(a) and (b), as well as Tables 5 and 6.

For the P case, $E_{cK} = \min\{1165, 835 + h\}$ meV, $E_{cK'} = E_{cK'\uparrow} = 835$ meV, $E_{c\uparrow} = E_{cK'\uparrow} = 835$ meV, $E_{c\downarrow} = E_{cK\downarrow} = 835 + h$ meV, as seen in Fig. 8(a) and (b) and Table 5. For the P case, $P_{KK'} = -1$ in the energy region $[835, \min\{835 + h, 1165\}$ meV], as shown in Fig. 8(c). When $300 < h < 330$ meV, it increases with h. When $h \geq 330$ meV, it remains at [835,1165 meV], with a width of 330 meV. $P_s = 1$ in the energy region $[835, 835 + h$ meV], which increases with h, as seen in Fig. 8(d).

For the AP case, $E_{cK\uparrow} = E_g + 2\lambda_c + h = 865 + h$ meV, and increases with h, as seen in Fig. 7(b) and Table 6. So $E_{cK} = E_{cK\downarrow} = 835 + h$ meV, $E_{cK'} = E_{cK'\uparrow} = 835 + h$ meV, $E_{c\uparrow} = E_{cK'\uparrow} = 835 + h$ meV, $E_{c\downarrow} = E_{cK\downarrow} = 835 + h$ meV, as seen in Fig. 8(e) and (f) and Table 6. For the AP case, the energy region with $P_{KK'} = -1$ ($P_s = 1$) does not exist, as seen in Fig. 8(g), (h).

Therefore, when $h \geq 300$ meV, TMR = 1 in the energy region $[835, 835 + h$ meV], which increases with h, as seen in Fig. 9(e) and (f).

Conclusion

In conclusion, by tuning the exchange field h in the FM region, the electrostatic potential U and CPL intensity $\Delta\Omega$ in the barrier region, the energy region of full spin and valley polarizations as well as large TMR in the F/B/N/B/F WSe$_2$ junction can be modulated, and the underlying physical mechanisms have been unveiled. We have derived the minimum incident energy of non-zero spin- and valley-resolved conductance, which is demonstrated by numerical calculations. The sign of the valley polarization $P_{KK'}$ depends on the helicity of the CPL, which does not happen to TMR and P_s. The energy region with TMR = 1 increases with h rapidly, remains unchanged first and then decreases as U increases, and has little dependence on $\Delta\Omega$. The energy region with $P_{KK'} = -1$ or $P_s = 1$ for the P case is much wider than that of the AP case, and they both increase evidently with $\Delta\Omega$. With increasing h, the $P_s = 1$ plateau widens for the P configuration, while the $P_{KK'} = -1$ or $P_s = 1$ plateau narrows for the AP configuration. For the P configuration, as U increases, the energy region with $P_{KK'} = -1$ ($P_s = 1$) increases (decreases) and that of $P_s = 1$ ($P_{KK'} = -1$) remains unchanged when U is relatively small (large). When U increases to a certain degree, the plateaus with $P_{KK'} = -1$ or $P_s = 1$ move parallel to the E_F-axis, regardless of P or AP configuration. Our research helps the practical application of ferromagnetic WSe$_2$ double-barrier junctions in fabricating spin-valleytronic and TMR devices.

Data availability

Data will be made available on request.

References

1. Novoselov, K. S. et al. Two-dimensional atomic crystals. *Proc. Natl. Acad. Sci. USA* **102**, 10451 (2005).
2. Lee, C. K. S. et al. Frictional characteristics of atomically thin sheets. *Science* **328**, 76 (2010).
3. Mak, K. F., Lee, C., Hone, J., Shan, J. & Heinz, T. F. Atomically thin MoS$_2$: A new direct-gap semiconductor. *Phys. Rev. Lett.* **105**, 136805 (2010).
4. Luo, L., Wang, S., Zheng, J. & Guo, Y. Spin- and valley-resolved tunneling magnetoresistance in a ferromagnetic transition metal dichalcogenide planar heterojunction modulated by polarized light. *Phys. Rev. B* **108**, 075434 (2023).
5. Xu, X., Yao, W., Xiao, D. & Heinz, T. F. Spin and pseudospins in layered transition metal dichalcogenides. *Nat. Phys.* **10**, 343 (2014).
6. Xiao, D., Liu, G. B., Feng, W., Xu, X. & Yao, W. Coupled Spin and Valley Physics in Monolayers of MoS$_2$ and Other Group-VI Dichalcogenides. *Phys. Rev. Lett.* **108**, 196802 (2012).
7. Lu, H. Z., Yao, W., Xiao, D. & Shen, S. Q. Intervalley scattering and localization behaviors of spin-valley coupled Dirac fermions. *Phys. Rev. Lett.* **110**, 016806 (2013).
8. Bertoni, R. et al. Generation and evolution of spin-, valley-, and layer-polarized excited carriers in inversion-symmetric WSe$_2$. *Phys. Rev. Lett.* **117**, 277201 (2016).
9. Tahir, M., Krstajić, P. M. & Vasilopoulos, P. Magnetic and electric control of spin- and valley-polarized transport across tunnel junctions on monolayer WSe$_2$. *Phys. Rev. B* **95**, 235402 (2017).
10. Jones, A. M. et al. Optical generation of excitonic valley coherence in monolayer WSe$_2$. *Nat. Nanotechnol.* **8**, 634 (2013).
11. Zhu, Z. Y., Cheng, Y. C. & Schwingenschlögl, U. Giant spin-orbit-induced spin splitting in two-dimensional transitionmetal dichalcogenide semiconductors. *Phys. Rev. B* **84**, 153402 (2011).
12. Hao, X. J., Yuan, R. Y., Ji, T. & Guo, Y. Switch effect for spin-valley electrons in monolayer WSe$_2$ structures subjected to optical field and Fermi velocity barrier. *J. Appl. Phys.* **128**, 154303 (2020).
13. MacNeill, D. et al. Breaking of valley degeneracy by magnetic field in monolayer MoSe$_2$. *Phys. Rev. Lett.* **114**, 037401 (2015).

14. Scharf, B., Xu, G., Matos-Abiague, A. & Žutič, I. Magnetic proximity effects in transition-metal dichalcogenides: Converting excitons. *Phys. Rev. Lett.* **119**, 127403 (2017).
15. Wang, Z., Tang, C., Sachs, R., Barlas, Y. & Shi, J. Proximity-induced ferromagnetism in graphene revealed by the anomalous Hall effect. *Phys. Rev. Lett.* **114**, 016603 (2015).
16. Saxena, R., Saha, A. & Rao, S. Conductance, valley and spin polarizations, and tunneling magnetoresistance in ferromagnetic-normal-ferromagnetic junctions of silicene. *Phys. Rev. B* **92**, 245412 (2015).
17. Wang, D., Huang, Z., Zhang, Y. & Jin, G. Spin-valley filter and tunnel magnetoresistance in asymmetrical silicene magnetic tunnel junctions. *Phys. Rev. B* **93**, 195425 (2016).
18. Qiu, X. J., Cao, Z. Z., Hou, J. & Yang, C. Y. Controlled giant magnetoresistance and spin–valley transport in an asymmetrical MoS$_2$ tunnel junction. *Appl. Phys. Lett.* **117**, 102401 (2020).
19. Lu, W. T., Tian, H. Y., Liu, H. M., Li, Y. F. & Li, W. Spin- and valley-dependent negative magnetoresistance in a ferromagnetic MoS$_2$ junction with a quantum well. *Phys. Rev. B* **98**, 075405 (2018).
20. Lazič, P., Belashchenko, K. D. & Žutič, I. Effective gating and tunable magnetic proximity effects in two-dimensional heterostructures. *Phys. Rev. B* **93**, 241401(R) (2016).
21. Zhao, C. et al. Enhanced valley splitting in monolayer WSe$_2$ due to magnetic exchange field. *Nat. Nanotechnol.* **12**, 757 (2017).
22. Liu, D., Liu, B., Yuan, R., Zheng, J. & Guo, Y. Valley filter and valley valve based on WSe$_2$ double-barrier junctions modulated by polarized light. *Phys. Rev. B* **103**, 245432 (2021).
23. Cao, T. et al. Valley-selective circular dichroism of monolayer molybdenum disulphide. *Nat. Commun.* **3**, 887 (2012).
24. Mak, K. F., He, K., Shan, J. & Heinz, T. F. Control of valley polarization in monolayer MoS$_2$ by optical helicity. *Nat. Nanotechnol.* **7**, 494 (2012).
25. Zeng, H. L., Dai, J. F., Yao, W., Xiao, D. & Cui, X. D. Valley polarization in MoS$_2$ monolayers by optical pumping. *Nat. Nanotechnol.* **7**, 490 (2012).
26. Qi, F. H., Cao, J. & Jin, G. J. Valley-controlled nonlocal transistor based on irradiated and biased bilayer graphene. *Phys. Rev. B* **98**, 045422 (2018).
27. Qiu, X. J., Cao, Z. Z., Lei, J. M., Shen, J. & Qin, C. C. Optical and electric control of charge and spin-valley transport in ferromagnetic silicene junction. *Superlatt. Microstruct.* **109**, 735 (2017).
28. Qiu, X., Lv, Q. & Cao, Z. Optical, electric and magnetic controlled ballistic conductance in monolayer WSe$_2$: the perfect valley and spin polarizations. *J. Phys. D: Appl. Phys.* **50**, 455106 (2017).
29. Yang, Q., Yuan, R. & Guo, Y. Valley switch effect based on monolayer WSe$_2$ modulated by circularly polarized light and valley Zeeman field. *J. Phys. D: Appl. Phys.* **52**, 335301 (2019).
30. Tahir, M., Manchon, A. & Schwingenschlögl, U. Photoinduced quantum spin and valley Hall effects, and orbital magnetization in monolayer MoS$_2$. *Phys. Rev. B* **90**, 125438 (2014).
31. Moodera, J. S., Kinder, L. R., Wong, T. M. & Meservey, R. Large magnetoresistance at room temperature in ferromagnetic thin film tunnel junctions. *Phys. Rev. Lett.* **74**, 3273 (1995).
32. Butler, W. H. Tunneling magnetoresistance from a symmetry filtering effect. *Sci. Technol. Adv. Mater.* **9**, 014106 (2008).
33. Maehara, H. et al. Tunnel magnetoresistance above 170% and resistance–area product of 1 (μm) 2 attained by in situ annealing of ultra-thin MgO tunnel barrier. *Appl. Phys. Express* **4**, 033002 (2011).
34. Zou, J., Jin, G. & Ma, Y. Q. Negative tunnel magnetoresistance and spin transport in ferromagnetic graphene junctions. *J. Phys.: Condens. Matter* **21**, 126001 (2009).
35. Bai, C. & Zhang, X. Large oscillating tunnel magnetoresistance in ferromagnetic graphene single tunnel junction. *Phys. Lett. A* **372**, 725 (2008).
36. Khezerlou, M. & Goudarzi, H. Valley permitted Klein tunneling and magnetoresistance in ferromagnetic monolayer MoS$_2$. *Superlatt. Microstruct.* **86**, 243 (2015).
37. Hajati, Y., Amini, Z. & Sabaeian, M. Controllable photoenhanced spin- and valley-polarized transport in ferromagnetic MoS$_2$ junction. *J. Magn. Magn. Mater.* **503**, 166580 (2020).
38. Chantngarm, P., Yamada, K. & Soodchomshom, B. Polarized-photon frequency filter in double-ferromagnetic barrier silicene junction. *J. Magn. Magn. Mater.* **429**, 16–22 (2017).
39. Hajati, Y. & Alipourzadeh, M. Spin- and valley-polarized transport and magnetoresistance in asymmetric ferromagnetic WSe$_2$ tunnel junctions. *Phys. Rev. B* **103**, 245435 (2021).
40. Hajati, Y., Alipourzadeh, M. & Makhfudz, I. Spin-valley dependent Klein tunneling and perfect spin- and valley-polarized transport in a magnetic WSe$_2$ superlattice. *Phys. Rev. B* **104**, 205402 (2021).
41. Hao, K. et al. Direct measurement of exciton valley coherence in monolayer WSe$_2$. *Nat. Phys.* **12**, 677 (2016).
42. Tahir, M. Electrical and optical transport properties of single layer WSe$_2$. *Physica E* **97**, 184–190 (2018).
43. Luo, L., Wang, S., Zheng, J. & Guo, Y. Optically controlled valley filter and transistor based on transition-metal Dichalcogenide planar heterojunctions. *Phys. Rev. APPL.* **18**, 044020 (2022).
44. Büttiker, M. Four-terminal phase-coherent conductance. *Phys. Rev. Lett.* **57**, 1761 (1986).
45. Fujita, T., Jalil, M. & Tan, S. Valley filter in strain engineered graphene. *Appl. Phys. Lett.* **97**, 043508 (2010).
46. Nguyen, V. H., Bournel, A. & Dollfus, P. Spin-polarized current and tunneling magnetoresistance in ferromagnetic gate bilayer graphene structures. *J. Appl. Phys.* **109**, 073717 (2011).

Acknowledgements

Author contributions

Ming Li: Conceptualization, Funding acquisition, Writing-review & editing. Zheng-Yin Zhao: Methodology, Writing-review & editing. Jia-Yi Sheng: Investigation, Writing-original draft.

Declarations

Competing interests

The authors declare that they have no known competing financial interests or personal relationships that could have appeared to influence the work reported in this paper.

Additional information

Correspondence and requests for materials should be addressed to M.L.

Reprints and permissions information is available at www.nature.com/reprints.